ELSEVIER

Large strain elasto-plastic model of paper and corrugated board

Anders Harrysson, Matti Ristinmaa [*]

Division of Solid Mechanics, Lund University, Box 118, S-221 00 Lund, Sweden

Abstract

An anisotropic elasto-plastic constitutive model of paper material is presented. It is formulated in a spatial setting in which anisotropic properties are accounted for by use of structural variables. A multiplicative split of the deformation gradient is employed to introduce plasticity. A similar approach is used to model the plastic deformation of the substructure. The yield surface adopted is based on the Tsai–Wu failure criterion, used previously to model failure of paper material. A non-associated plasticity theory is employed to calibrate the model to experimental data. It turns out that a multi-axial loading situation is needed to calibrate the model and here a biaxial tension test is audited. The model was implemented into a finite element environment and the creasing process of a corrugated board panel is investigated.
© 2008 Elsevier Ltd. All rights reserved.

Keywords: Plasticity; Anisotropy; Paper material; Thermodynamics; Finite strains

1. Introduction

Packaging paper is a generic name for paper material of all types used for packaging goods. The material known as corrugated board is produced by a converting process in which two or more layers are laminated, cf. Fig. 1. The flat top and bottom layers are called liners and the corrugated core is referred to as fluting. Corrugated board is frequently used for making boxes for the transport of goods and the like, is one of the most used packaging material. Its low cost per unit weight, the possibility of recycling and the high stiffness per unit weight makes it an attractive material. During the lifetime of a package, the material of which it is constructed will be exposed to mechanical loading during for instance transportation and storage. In the past, attempts have been made to predict the load-carrying capacity of corrugated box, cf. the pioneer work by McKee et al. (1963). More recent work addressing this problem can be found in Patel et al. (1997), Nyman (2000) and Nordstrand et al. (2003). Still more recently in the work of Biancolini (2005) and Isaksson and Hägglund (2005) the finite element method was used to gain better understanding of how a corrugated board panel deforms during sever mechanical loading. It has been found that even during the box manufacturing process itself the corrugated board may be severely deformed, particularly in the folding areas. The modeling of this process will be considered here and therefore a material model for paper will be the main concern in this paper.

---

[*] Corresponding author. Fax: +46 46 2223115.
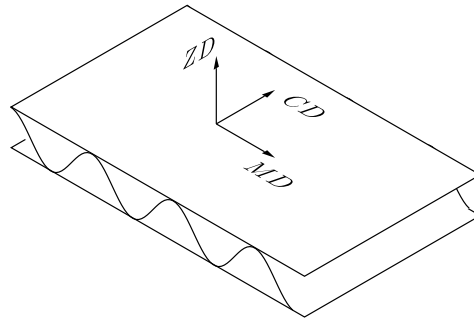*E-mail address:* Matti.Ristinmaa@solid.lth.se (M. Ristinmaa).

Fig. 1. Single wall corrugated board panel. The material directions of the paper are indicated.

The main building blocks of packaging paper are cellulose fibers, consisting primary of wood fibers, although other materials are sometimes employed as well. The manufacturing process usually involves the dewatering of a cellulose fiber suspension on a web. The fibers have the inherent capability of bonds being formed between them without the use of any additives. Due to the manufacturing of the separate paper layers, the fibers tend to become aligned to the direction in which the web is running. This direction is usually referred to as the machine direction (MD). The direction perpendicular to this direction in the plane of the web is called the cross direction (CD). The third direction is the out-of-plane direction (ZD), cf. Fig. 2. The strength of the bonds and the longitudinal properties of the fibers are the main factors for the in-plane mechanical properties of the paper sheet. The mechanical properties in the out-of-plane direction are related to the fiber properties perpendicular to the longitudinal direction and the bond strength. Due to the orientation of the fibers in the paper material, the mechanical response will differ depending upon the loading direction. Since the fibers tend to become oriented in the MD direction this direction also is the 'strongest' direction, i.e. higher Young's modulus, yield stress etc. The material properties in CD are about two to four times lower than in MD. Since the in-plane and out-of-plane mechanical properties are governed by rather different physical mechanisms, the mechanical out-of-plane properties are very different from the in-plane properties. Stiffness and yield stress are of the order of two lower than the in-plane properties.

As known from material testing, cf. Steenberg (1949), paper show a highly non-linear response even when exposed to only moderate deformations. One can note as well that unloading from the non-linear region introduces non-recoverable strains. Such observations motivate the use of plasticity theory. Further and very important factor when modeling paper material are the directional dependent properties. Attempts to model the mechanical properties of paper material have been made recently by Castroa and Ostoja-Starzewski (2003) as well as Xia et al. (2002) and Mäkelä and Östlund (2003) who considered elasto-plastic properties of paper and Isaksson et al. (2004) how also considered damage.

The present study takes up a large strain elasto-plastic material model of paper based on an orthotropic hyperelastic model, orthotropic yield surface and hardening model. To account for the different yield stresses in tension and compression, an approach similar to that of Shih and Lee (1978) has been adopted. However, since paper do
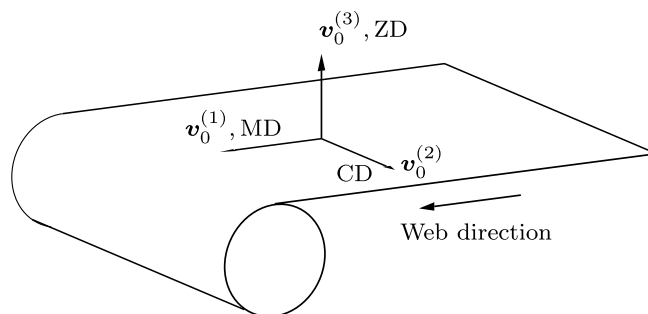

Fig. 2. Illustrations of the different material directions of a single material layer due to manufacturing process. Here $v_0^{(1)}$, $v_0^{(2)}$ and $v_0^{(3)}$ denotes the base vectors defining the directions corresponding to MD, CD and ZD, respectively.

not show proof of plastic incompressibility, the calibration becomes much more involved. For introducing orthotropic material properties into the constitutive model, here, use has been made of structural tensors, cf. Boehler (1987). This approach has been used in connection with both the elastic and the plastic part of the model. The framework will in addition allow for evolving anisotropy, but this subject will not be pursued further.

Before development of the model itself is taken up, experimental findings obtained for the paper material that was investigated will be presented. Then the theoretical foundation of the proposed model will be discussed as well as the corresponding calibration procedure. Finally, numerical examples will be presented where the creasing operation of a corrugated board will be considered.

1.1. Experimental evidence

Experiments on a material with grammage of 150 g/m² and thickness of 0.32 mm where conducted in a controlled environment held at a temperature of 23 °C and a relative humidity of 50%. The curves represents mean values from test samples containing five tests in every test case. Furthermore, a low strain rate of 0.8 mm/min was used. The different uniaxial stress–strain curves for the in-plane loading of paper in MD, 45° and CD are shown in Fig. 3(a). The curves terminate at the point where fracture has taken place. The stress–strain relation is rather linear during the first, elastic, part of the deformation, but after a certain stress value has been reached, the response becomes non-linear. The different loading directions clearly reveals the strong anisotropy that is present in paper. The result from successive loading and unloading are shown in Fig. 3(b). It is clear that some part of the deformation do not recover, motivating the need of modeling plastic behavior. The response also reveals a Baushinger effect to be present. This is known to exist for this type of material, cf. Sawyer et al. (1996). Furthermore, regarding physical explanation of the plastic behavior, Seth and Page (1983) showed experimentally that the plasticity of paper is mainly caused by the plasticity of fibres and the effect of bond breakage is usually small. From Fig. 4 it is observed that the ratio axial/lateral strain can be considered as constant during uniaxial tension loading conditions. Furthermore, this also indicated that the ratio of axial/lateral plastic strain is constant. The response of biaxial proportional tension loading is shown in Fig. 5. There the forces, F_{MD} and F_{CD} acting in MD and CD, respectively, are equal in these two to each other perpendicular directions. A compression test was performed to evaluate the properties connected with the out-of-plane direction of the paper. The result can be seen in Fig. 6. As already indicated, and evident from Fig. 3(b), both elastic and plastic deformations are present. As noted in experiments, the out-of-plane deformation is both elastic and plastic, cf. Stenberg et al. (2001b). In the corrugated board applications considered here it is sufficient to assume, however, that the out-of-plane deformation is purely elastic.

A glance of the results of the uniaxial tests reveals no clear yielding point can be identified. To locate the yielding point, the assumption of linear-elastic behavior is used. This allows the yielding point to be located at the point where the stress–strain curve deviates from the linear stiffness found initial. For orthotropic materials the initial flexibility matrix, given in Voigt notation, can be written as

(a) Directionally dependent properties of paper
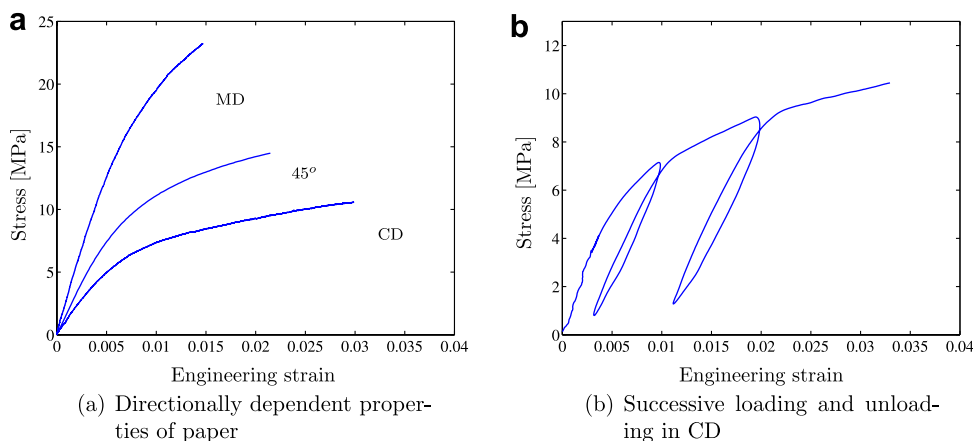
(b) Successive loading and unloading in CD

Fig. 3. Results of uniaxial tension loading: (a) in MD, CD and 45° and (b) testing in CD direction under successive loading and unloading.
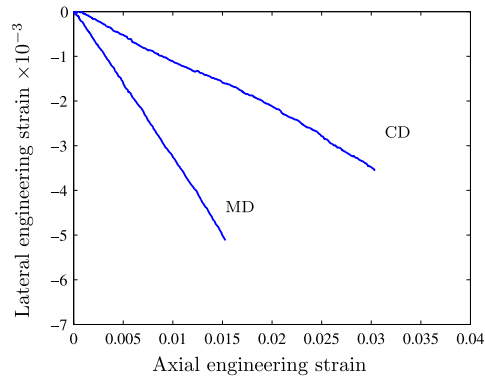
Fig. 4. Axial vs. lateral strain during uniaxial tension loading in MD and CD.
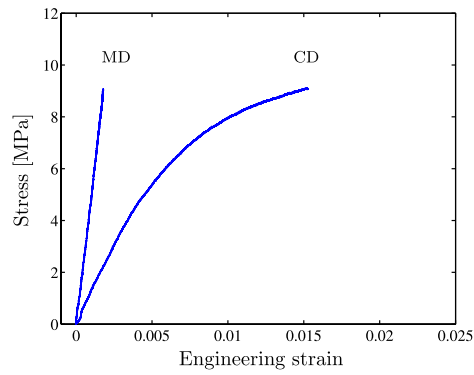
Fig. 5. Result from biaxial tension testing, loading ratio $F_{MD}/F_{CD} = 1$.
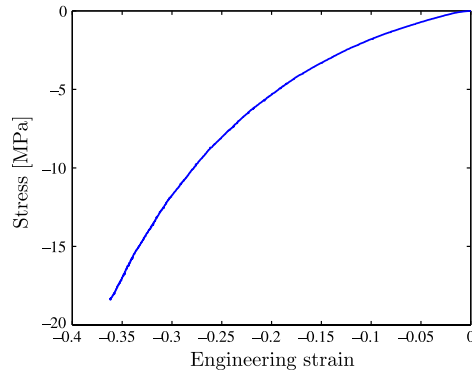
Fig. 6. Result from compression test in ZD.

$$[\mathcal{C}] = \begin{bmatrix} \frac{1}{E_1} & -\frac{v_{21}}{E_2} & -\frac{v_{31}}{E_3} & 0 & 0 & 0 \\ -\frac{v_{12}}{E_1} & \frac{1}{E_2} & -\frac{v_{32}}{E_3} & 0 & 0 & 0 \\ -\frac{v_{13}}{E_1} & -\frac{v_{23}}{E_2} & \frac{1}{E_3} & 0 & 0 & 0 \\ 0 & 0 & 0 & \frac{1}{G_{12}} & 0 & 0 \\ 0 & 0 & 0 & 0 & \frac{1}{G_{13}} & 0 \\ 0 & 0 & 0 & 0 & 0 & \frac{1}{G_{23}} \end{bmatrix} \tag{1}$$

where the components are ordered according to [11 22 33 12 13 23]. The indices on the material properties are related to the bases $\mathbf{v}_0^{(\alpha)}$, cf. Fig. 2. Assuming the existence of a strain energy function, the relations $v_{12}/E_1 = v_{21}/E_2$, $v_{13}/E_1 = v_{31}/E_3$ and $v_{23}/E_2 = v_{32}/E_3$ hold, i.e. $\mathcal{C}$ is symmetric. From Figs. 3 and 4 it is concluded that the in-plane symmetry condition is fulfilled.

The in-plane elastic properties of the paperboard examined here are categorizes by standard quantities (Young's modulus, Poisson's ratio and shear modulus). Young's modulus can be determined from Fig. 3(a) and Poisson's ratio can be established from Fig. 4. Unfortunately, the shear modulus cannot easily be measured directly. However, since data in 45°-direction exist, using Young's modulus obtained from an uniaxial test in 45°-direction, the in-plane shear modulus, G_{12} can be calculated using a coordinate transformation. The elastic constant related to out-of-plane direction, i.e. E_{33}, G_{13} and G_{23} and Poisson's ratios v_{13} and v_{23} are not straightforward to measure, cf. Stenberg (2003). Therefore the values obtained by Baum (1985) will be used. In summary the elastic properties are given as

$$E_{11} = 3050 \text{ MPa}, \quad E_{22} = 1172 \text{ MPa}, \quad E_{33} = 35 \text{ MPa}$$
$$G_{12} = 720 \text{ MPa}, \quad G_{13} = 10 \text{ MPa}, \quad G_{23} = 10 \text{ MPa} \tag{2}$$
$$v_{12} = 0.3, \quad v_{13} = 0.01, \quad v_{23} = 0.01$$

Considering properties related to initial yielding, analysing the experimental data discussed earlier, the following data related to initial yielding can be found (all in MPa)

$$\tau_{\text{MD},t} = 7, \quad \tau_{\text{MD},c} = 4, \quad \tau_{\text{CD},t} = 3$$
$$\tau_{\text{CD},c} = 3, \quad \tau_{45} = 7, \quad \tau_b = 3.3 \tag{3}$$

Here $\tau_{\text{MD},t}$, $\tau_{\text{MD},c}$, $\tau_{\text{CD},t}$, $\tau_{\text{CD},c}$, τ_{45} and τ_b are the yield stresses in MD tension/compression and CD tension/compression, yield stress in 45° and in biaxial loading situation, respectively. To obtain the data related to compression an investigation of the response during compression loading is called for. The standard short compression test (SCT), cf. Cavlin and Fellers (1975), was used in these investigations. Data from the SCT, which only provided the ultimate load level, were used to estimate the initial yield stresses in compression. To estimate the initial yield stresses a simple scaling of the SCT values by a factor 1/4 was used. Moreover, due to lack of stress–strain curves in compression, it will be assumed that after yielding takes place in compression an ideal plastic response is obtained.

2. Model development

2.1. Kinematic description

Consider first a brief description of the kinematic quantities. Let $\Omega_0 \subset \mathbb{R}^3$ denote the reference configuration of a body and let a particle be identified via its position vector $X \in \Omega_0$. At time $t \in \mathbb{R}$ a smooth deformation is a one-to-one mapping (generally non-linear) $\boldsymbol{\varphi} : \Omega_0 \times t \to \Omega \subset \mathbb{R}^3$. The motion of the particle labeled $X \in \Omega_0$ is then identified via $x = \boldsymbol{\varphi}(X, t)$, $x \in \Omega$, is the position vector of a particle in the current configuration Ω. The deformation of the body at a fixed time can be identified by reference to the linear map of a vector in the tangent space $T\Omega_0$ to a vector in the tangent space $T\Omega$, i.e. $\boldsymbol{F} = \partial_X \boldsymbol{\varphi}_t$ where $\boldsymbol{F}$ is known as the deformation gradient. To make the map unique, it is required that $J = \det(\boldsymbol{F}) > 0$. From this assumption, it follows that the deformation gradient is non-singular.

Time derivation of the deformation gradient allows the spatial velocity gradient to be defined, such that

$$\dot{\boldsymbol{F}} = \boldsymbol{L}\boldsymbol{F} \tag{4}$$

The spatial velocity gradient may be split into a symmetric and a skew-symmetric part according to

$$\boldsymbol{L} = \text{sym}[\boldsymbol{L}] + \text{skew}[\boldsymbol{L}] = \boldsymbol{D} + \boldsymbol{W} \tag{5}$$

Here $\text{sym}[\cdot] = \frac{1}{2}([\cdot] + [\cdot]^T)$ and $\text{skew}[\cdot] = \frac{1}{2}([\cdot] - [\cdot]^T)$, denote the symmetric and skew-symmetric part of a second-order tensor, respectively, and $\boldsymbol{D}$ and $\boldsymbol{W}$ are known as the rate of deformation tensor and the spin tensor, respectively.

So far, no specific quantity has been introduced for describing any directionally dependent properties of the material, i.e. the substructure of the material which for this particular material is defined by the fiber orientation. Following Harrysson and Ristinmaa (2007), for this purpose, a set of vectors $\boldsymbol{v}_0^{(\alpha)}$ is introduced in the reference configuration, cf. also Fig. 2. These vectors describe in a phenomenological sense the directionally dependent properties of the material. A similar set of vectors $\boldsymbol{v}^{(\alpha)}$ is introduced in the current configuration and the two sets of vectors are related according to the linear map

$$\boldsymbol{v}^{(\alpha)} = \boldsymbol{\Delta}^{(\alpha)} \boldsymbol{v}_0^{(\alpha)} \tag{6}$$

Here the superscript (α) indicate different director vectors and it is noted that the linear maps $\boldsymbol{\Delta}^{(\alpha)}$ may be different for each director vector. From (6) it is clear that $\boldsymbol{\Delta}^{(\alpha)}$ represents a linear map in the same sense as the deformation gradient, but acting on the substructure and not on the continuum. This quantity is called substructural deformation gradient.

In modeling large strain plasticity, the deformation gradient and the substructural deformation gradient need to be investigated further to be able to distinguish between elastic and plastic deformation. For this purpose, the multiplicative split of the deformation gradient is adopted, cf. Kröner (1960) and Lee (1969). The elastic and plastic parts of the deformation are then identified as

$$\boldsymbol{F} = \boldsymbol{F}^e \boldsymbol{F}^p \tag{7}$$

where $\boldsymbol{F}^e$ and $\boldsymbol{F}^p$ denote the elastic and plastic parts of the deformation gradient, respectively. More precisely, a line segment is first mapped into an unstressed intermediate configuration, denoted $\overline{\Omega}$, by the plastic part, $\boldsymbol{F}^p$ of the deformation gradient. This line segment is then subsequently mapped from the unstressed configuration to the current configuration by the elastic part of the deformation gradient, $\boldsymbol{F}^e$. Hence, a geometrical decoupling between elastic and plastic deformation is achieved. A similar approach can be taken for the substructure according to

$$\boldsymbol{\Delta} = \boldsymbol{\beta}^{(\alpha)} \boldsymbol{\alpha}^{(\alpha)} \tag{8}$$

where $\boldsymbol{\alpha}^{(\alpha)}$ maps the director vectors from the reference configuration, $\boldsymbol{v}_0^{(\alpha)}$, to the intermediate configuration, $\overline{\boldsymbol{v}}^{(\alpha)}$, and $\boldsymbol{\beta}^{(\alpha)}$ subsequently maps the director vectors from the intermediate configuration to the current configuration, $\boldsymbol{v}^{(\alpha)}$, see Fig. 7. In this sense $\boldsymbol{\alpha}^{(\alpha)}$ is related to the plastic deformation and $\boldsymbol{\beta}^{(\alpha)}$ is related to the elastic deformation. Note that some additional assumption is required concerning a link between (7) and (8), the continuum and the substructure, respectively, a matter that will be discussed later. Since an arbitrary rotation may be added to the intermediate configuration, and still be stress free, this configuration is not uniquely determined, cf. Dafalias (1986) or the discussion of Harrysson and Ristinmaa (2007). However, if a spatial setting
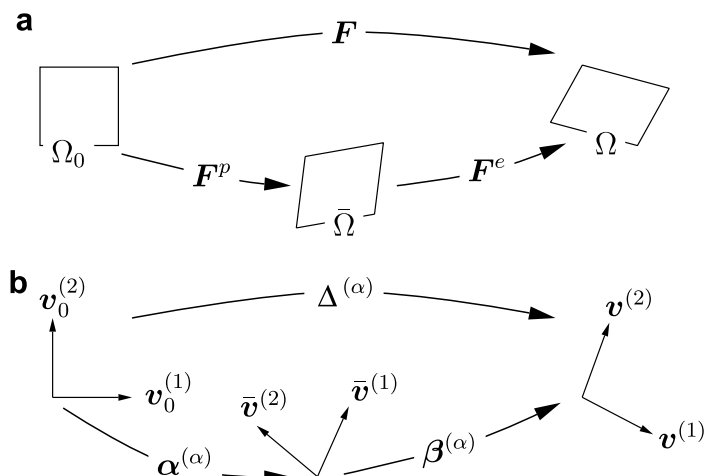

Fig. 7. Deformation of the (a) continuum and (b) the substructure.

is adopted, the arbitrary orientation of the intermediate configuration will not enter the model description as shown in Harrysson et al. (2007)

Returning to the continuum, the evolution of the elastic and the plastic deformation gradient can be establish in a similar manner as (4), i.e.

$$\dot{\boldsymbol{F}}^e = \boldsymbol{L}^e \boldsymbol{F}^e; \quad \dot{\boldsymbol{F}}^p = \boldsymbol{l}^p \boldsymbol{F}^p \tag{9}$$

where $\boldsymbol{L}^e$ is the elastic velocity gradient and $\boldsymbol{l}^p$ is the plastic velocity gradient, respectively. The total velocity gradient can be constructed using (9) as

$$\boldsymbol{L} = \boldsymbol{L}^e + \boldsymbol{F}^e \boldsymbol{l}^p \boldsymbol{F}^{e-1} = \boldsymbol{L}^e + \boldsymbol{L}^p \tag{10}$$

where $\boldsymbol{L}^e$ is a spatial quantity and $\boldsymbol{L}^p$ is the spatial representation of $\boldsymbol{l}^p$. For the substructure, similar expressions can be established for the elastic and plastic part of the substructural velocity gradient. Following the approach of Harrysson and Ristinmaa (2007) gives

$$\dot{\boldsymbol{\beta}}^{(\alpha)} = \boldsymbol{\Gamma}^{(\alpha)} \boldsymbol{\beta}^{(\alpha)}; \quad \dot{\boldsymbol{\alpha}}^{(\alpha)} = \boldsymbol{\Lambda}^{(\alpha)} \boldsymbol{\alpha}^{(\alpha)} \tag{11}$$

where $\boldsymbol{\Gamma}^{(\alpha)}$ is the elastic velocity gradient and $\boldsymbol{\Lambda}^{(\alpha)}$ is the plastic velocity gradient acting on the substructure, respectively. In analogy to (10) a total velocity gradient acting on the substructure can be established according to

$$\dot{\boldsymbol{\Delta}} \boldsymbol{\Delta}^{-1} = \boldsymbol{\Gamma}^{(\alpha)} + \boldsymbol{\beta}^{(\alpha)} \boldsymbol{\Lambda}^{(\alpha)} \boldsymbol{\beta}^{(\alpha)-1} \tag{12}$$

Next a connection between the continuum and the substructure must be introduced. From a physical point of view, it is assumed that the substructure and the continuum deforms together in a convected sense if purely elastic deformation is considered. This leads to the constitutive assumption that

$$\boldsymbol{\beta}^{(\alpha)} = \boldsymbol{F}^e \tag{13}$$

For use further on the evolution equations are established in a spatial setting. Consider first the elastic deformation of the continuum. This can be represented by the elastic Finger deformation tensor

$$\boldsymbol{b}^e = \boldsymbol{F}^e \boldsymbol{F}^{eT} \tag{14}$$

Time differentiation of (14), with use of (10) results then in

$$\dot{\boldsymbol{b}}^e = \boldsymbol{L} \boldsymbol{b}^e + \boldsymbol{b}^e \boldsymbol{L}^T - (\boldsymbol{L}^p \boldsymbol{b}^e + \boldsymbol{b}^e \boldsymbol{L}^{pT}) \tag{15}$$

Proceeding in a similar fashion with the substructure, evolution equation for the preferred directions has to be established. Starting with the assumption of elastic convectivity (13), it follows that $\bar{\boldsymbol{v}}^{(\alpha)} = \boldsymbol{\alpha}^{(\alpha)} \boldsymbol{v}_0^{(\alpha)}$ and $\boldsymbol{v}^{(\alpha)} = \boldsymbol{F}^e \bar{\boldsymbol{v}}^{(\alpha)}$. Time differentiation of latter relation with use of (10) and (11) then gives

$$\dot{\boldsymbol{v}}^{(\alpha)} = \boldsymbol{L} \boldsymbol{v}^{(\alpha)} + (\boldsymbol{\lambda}^{(\alpha)} - \boldsymbol{L}^p) \boldsymbol{v}^{(\alpha)} \tag{16}$$

where a spatial representation of $\boldsymbol{\Lambda}^{(\alpha)}$ was introduced in the form of $\boldsymbol{\lambda}^{(\alpha)} = \boldsymbol{F}^e \boldsymbol{\Lambda}^{(\alpha)} \boldsymbol{F}^{e-1}$ To proceed, evolution laws needs to be assigned to $\boldsymbol{L}^p$ and $\boldsymbol{\lambda}^{(\alpha)}$ in a consistent fashion. This is done in the section that follows, by use of thermodynamic relations.

2.2. Thermodynamic relations

The second law of thermodynamics introduces a formal requirement placed on the constitutive model describing the material behavior. The second law of thermodynamics is usually transformed into the dissipation inequality, cf. Truesdell and Noll (1965), which for isothermal conditions is given by,

$$\gamma = \boldsymbol{\tau} : \boldsymbol{D} - \rho_0 \dot{\psi} \geqslant 0 \tag{17}$$

where ψ is the Helmholtz free energy function and ρ_o is the mass density in the reference configuration. Furthermore, $\boldsymbol{\tau}$ is the Kirchhoff stress tensor and $\boldsymbol{D}$ is the rate of deformation tensor introduced earlier. The process is called reversible if $\gamma = 0$ (for instance elastic deformation) and irreversible if $\gamma > 0$ (for instance plastic

deformation). Thus for isothermal processes (17) should be fulfilled irrespective the material model considered.

Two ingredients are needed to characterize the state of the material which has undergone a plastic deformation: an elastic strain measure and the history of the plastic loading that has occurred. If both of these are known, the state of the material is likewise known. Returning to the Helmholtz free energy, it follows that

$$\psi = \psi(\boldsymbol{b}^e, \boldsymbol{m}^{(\alpha)}, \kappa_\beta), \quad \beta = 1, 2, \ldots, n \tag{18}$$

is a possible representation where κ_β are some internal variables that describe the history of plastic loading. In general, these can be tensors of different orders. For the situation considered here, however, it is assumed that κ_β are scalars. This is sufficient for describing the hardening of the material. In (18) $\boldsymbol{m}^{(\alpha)}$ is used for describing the anisotropic properties of the material and is constructed using the director vectors according to $\boldsymbol{m}^{(\alpha)} = \boldsymbol{v}^{(\alpha)} \otimes \boldsymbol{v}^{(\alpha)}$, cf. Liu (1982), Boehler (1987) and Spencer (1987). It is also noted that due to objectivity reasons it is required that ψ is an isotropic function of its argument, i.e. ψ can only be a function of invariants of $\boldsymbol{b}^e$ and $\boldsymbol{m}^{(\alpha)}$ and the joint invariants of $\boldsymbol{b}^e$ and $\boldsymbol{m}^{(\alpha)}$. Taking advantage of (18), the dissipation inequality can be rewritten as

$$\gamma = \boldsymbol{\tau} : \boldsymbol{D} - \rho_0 \frac{\partial \psi}{\partial \boldsymbol{b}^e} : \dot{\boldsymbol{b}}^e - \sum \rho_0 \frac{\partial \psi}{\partial \boldsymbol{m}^{(\alpha)}} : \dot{\boldsymbol{m}}^{(\alpha)} - \sum R_\beta \dot{\kappa}_\beta \geqslant 0 \tag{19}$$

where the conjugated forces R_β have been introduced according to

$$R_\beta = \rho_0 \frac{\partial \psi}{\partial \kappa_\beta} \tag{20}$$

To further evaluate (19) the time differentiation of the elastic Finger tensor and the structural tensors has to be introduced. The time differentiation of the Finger tensor are given by (15) and the time differentiation of the structural tensors can be evaluated using (16) and the definition of the structural tensors according to

$$\dot{\boldsymbol{m}}^{(\alpha)} = \boldsymbol{L}\boldsymbol{m}^{(\alpha)} + \boldsymbol{m}^{(\alpha)}\boldsymbol{L}^{\mathrm{T}} + (\boldsymbol{\lambda}^{(\alpha)} - \boldsymbol{L}^p)\boldsymbol{m}^{(\alpha)} + \boldsymbol{m}^{(\alpha)}(\boldsymbol{\lambda}^{(\alpha)} - \boldsymbol{L}^p) \tag{21}$$

Hence it follows that the dissipation inequality can be reformulated, yielding

$$\gamma = \left(\boldsymbol{\tau} - 2\rho_0 \frac{\partial \psi}{\partial \boldsymbol{b}^e} \boldsymbol{b}^e - 2\rho_0 \sum_\alpha \frac{\partial \psi}{\partial \boldsymbol{m}^{(\alpha)}} \boldsymbol{m}^{(\alpha)} \right) : \boldsymbol{L} + \left(2\rho_0 \frac{\partial \psi}{\partial \boldsymbol{b}^e} \boldsymbol{b}^e + 2\rho_0 \sum_\alpha \frac{\partial \psi}{\partial \boldsymbol{m}^{(\alpha)}} \boldsymbol{m}^{(\alpha)} \right) : \boldsymbol{L}^p$$
$$- 2\rho_0 \sum_\alpha \frac{\partial \psi}{\partial \boldsymbol{m}^{(\alpha)}} \boldsymbol{m}^{(\alpha)} : \boldsymbol{\lambda}^{(\alpha)} - \sum_\beta R_\beta \dot{\kappa}_\beta \geqslant 0 \tag{22}$$

Following the discussion in Harrysson et al. (2007) the symmetric Kirchhoff stress tensor can be introduced as

$$\boldsymbol{\tau} = 2\rho_0 \frac{\partial \psi}{\partial \boldsymbol{b}^e} \boldsymbol{b}^e + 2\rho_0 \sum_\alpha \frac{\partial \psi}{\partial \boldsymbol{m}^{(\alpha)}} \boldsymbol{m}^{(\alpha)} \tag{23}$$

cf. also Menzel and Steinmann (2003). By use of this definition in (22) it follows that

$$\gamma = \boldsymbol{\tau} : \boldsymbol{D}^p - \sum \boldsymbol{r}^{(\alpha)} : \boldsymbol{\lambda}^{(\alpha)} - \sum_\beta R_\beta \dot{\kappa}_\beta \geqslant 0 \tag{24}$$

where $\boldsymbol{D}^p = \mathrm{sym}(\boldsymbol{L}^p)$ is the plastic rate of deformation tensor and $\boldsymbol{r}^{(\alpha)}$ represents here a thermodynamic force, conjugated to $\boldsymbol{\lambda}^{(\alpha)}$, defined as

$$\boldsymbol{r}^{(\alpha)} = \frac{\partial \psi}{\partial \boldsymbol{m}^{(\alpha)}} \boldsymbol{m}^{(\alpha)} \tag{25}$$

It appears natural to divide the dissipation inequality into two separate parts, the one containing information of the continuum and the other containing information of the substructure. This can be done according to

$$\gamma = \gamma_{\mathrm{mech}} + \gamma_{\mathrm{sub}} \geqslant 0 \tag{26}$$

where γ_{mech} and γ_{sub} are introduced according to

$$\gamma_{\text{mech}} = \boldsymbol{\tau} : \boldsymbol{D}^p - \sum_\beta R_\beta \dot{\kappa}_\beta; \quad \gamma_{\text{sub}} = -\sum \boldsymbol{r}^{(\alpha)} : \boldsymbol{\lambda}^{(\alpha)} \tag{27}$$

Until this point, it has been stated that the dissipation inequality has to be satisfied for all loading conditions, and this will put certain restrictions on the constitutive model that is used. Here a conservative approach is used assuming that both parts of the dissipation inequality should be fulfilled separately, i.e. $\gamma_{\text{mech}} \geqslant 0$ and $\gamma_{\text{sub}} \geqslant 0$.

Consider first the mechanical part of the dissipation inequality, γ_{mech}. There are various ways for (27a) to be fulfilled. First, in order to determine whether plastic deformation has occurred, an elastic domain is introduced according to

$$\mathcal{E} = \{(\boldsymbol{\tau}, \boldsymbol{m}^{(\alpha)}, \bullet) | f(\boldsymbol{\tau}, \boldsymbol{m}^{(\alpha)}, \bullet) \leqslant 0\} \tag{28}$$

where ($\bullet$) denote additional quantities of relevance for the description, such as the effective plastic strain. The boundary of this domain is termed the yield surface.

The evolution laws are then found by considering a convex potential function, having the properties $g(\boldsymbol{\tau}, \boldsymbol{m}^{(\alpha)}, R_\beta) - g(\boldsymbol{0}, \boldsymbol{m}^{(\alpha)}, 0) \geqslant 0$. It then follows that $\gamma_{\text{mech}} \geqslant 0$ if the following evolution laws are given by

$$\begin{aligned} \boldsymbol{D}^p &= \lambda \frac{\partial g}{\partial \boldsymbol{\tau}} \\ \dot{\kappa}_\beta &= -\lambda \frac{\partial g}{\partial R_\beta} \end{aligned} \tag{29}$$

where λ is a positive plastic multiplier. In addition it is assumed that the loading conditions $f \leqslant 0$, $\lambda \geqslant 0$ and $f\lambda = 0$ holds. The evolution laws given in (29) is usually referred to as non-associated plasticity. The specific choice of $g = f$ results in the associative plasticity theory, consistent with the postulate of maximum plastic dissipation. It is also noted that different quantities can be used in the potential function and the yield function, advantage of this fact will be used later on in the calibration procedure, cf. also Ristinmaa et al. (2007). It is possible to use the same approach for fulfilling the dissipation inequality for the substructure γ_{sub} where a potential function $g_{\text{sub}} = g_{\text{sub}}(\boldsymbol{r}^{(\alpha)})$ with the same properties as above is introduced, i.e. the following evolution law is obtained

$$\boldsymbol{\lambda}^{(\alpha)} = \lambda \frac{\partial g_{\text{sub}}}{\partial \boldsymbol{r}^{(\alpha)}} \tag{30}$$

2.3. Specific model

The elastic part and the plastic part of the model are based on the concept of invariants formed by using structural tensors to describe the directional dependency of the material. To model the orthotropic behavior it is used that three orthogonal material directions are introduced in the reference configuration. These directions are described by MD, CD and ZD for the paper material, cf. Fig. 2. In addition to the assumption in (18) an additive split of Helmholtz' free energy is used according to

$$\psi = \psi^e(\boldsymbol{b}^e, \boldsymbol{m}^{(\alpha)}) + \psi^p(\kappa_\beta) \tag{31}$$

where κ_β are, as described previously, scalar internal variables used to incorporate hardening. The specific definition of the internal variables will be discussed in the sequel. The elastic part of the free energy is taken as

$$\rho_0 \psi^e = K \left(\frac{J^{e2} - 1}{2} - \ln(J^e) \right)^2 + \sum_{\alpha=1}^3 \frac{a_\alpha}{2} I_\alpha^{e2} + b_\alpha I_\alpha^e I_{\alpha+1}^e + c_\alpha J_\alpha^e \tag{32}$$

where it for simplicity was introduced that $I_4^e = I_1^e$, and the following invariants are used

$$\begin{aligned} I_\alpha^e &= \frac{1}{2}(\text{tr}[\boldsymbol{m}^{(\alpha)}] - 1), \quad J_\alpha^e = \frac{1}{4}\left(\boldsymbol{b}^e : \boldsymbol{m}^{(\alpha)} - 2\text{tr}[\boldsymbol{m}^{(\alpha)}] + 1\right) \\ J^e &= \det(\boldsymbol{b}^e)^{1/2} \end{aligned} \tag{33}$$

It is noted that the first term of the free energy function is a function describing the isotropic properties of the model. The reason for introducing this first term in (32) is to obtain a reasonable response in compression. It is emphasized that without this term, $\psi^e \to \infty$ as $J^e \to 0$ is not fulfilled, which is a growth condition of the strain energy function, here given by ψ^e, cf. Ciarlet (1988). The quadratic format is chosen such that it will not influence upon the initial tangent stiffness. Furthermore, it is here assumed that this term is only active during compression, i.e.

$$K = \begin{cases} K_b & \text{if } J^e < 1 \\ 0 & \text{otherwise} \end{cases} \tag{34}$$

Taking advantage of (32) in (23) it follows that the Kirchhoff stress tensor takes the form

$$
\begin{aligned}
\boldsymbol{\tau} = {} & K\left(\frac{J^{e2}-1}{2} - \ln(J^e)\right)(J^{e2}-1)\boldsymbol{I} + (a_1 I_1^e + b_1 I_2^e + b_3 I_3^e - c_1)\boldsymbol{m}^{(1)} \\
& + (b_1 I_1^e + a_2 I_2^e + b_2 I_3^e - c_2)\boldsymbol{m}^{(2)} + (b_3 I_1^e + b_2 I_2^e + a_3 I_3^e - c_3)\boldsymbol{m}^{(3)} \\
& + \frac{1}{2}c_1(\boldsymbol{b}^e \boldsymbol{m}^{(1)} + \boldsymbol{m}^{(1)} \boldsymbol{b}^e) + \frac{1}{2}c_2(\boldsymbol{b}^e \boldsymbol{m}^{(2)} + \boldsymbol{m}^{(2)} \boldsymbol{b}^e) + \frac{1}{2}c_3(\boldsymbol{b}^e \boldsymbol{m}^{(3)} + \boldsymbol{m}^{(3)} \boldsymbol{b}^e)
\end{aligned}
\tag{35}
$$

It is noted that (35) result in a stress free intermediate configuration, i.e. when $\boldsymbol{F}^e = \boldsymbol{I}$. The calibration of the model to experimental data is done by considering the initial tangential stiffness. The tangential stiffness in the spatial setting is defined by a push forward operation of the tangential stiffness in the material setting, according to

$$\boldsymbol{\mathcal{L}} = 2(\boldsymbol{F} \boxtimes \boldsymbol{F}) : \frac{\partial \boldsymbol{S}}{\partial \boldsymbol{C}} : \left(\boldsymbol{F}^{\mathrm{T}} \boxtimes \boldsymbol{F}^{\mathrm{T}}\right) \tag{36}$$

where in Cartesian components $(\boldsymbol{A} \boxtimes \boldsymbol{B})_{ijkl} = \frac{1}{2}(A_{ik} B_{jl} + A_{il} B_{jk})$ is introduced. Furthermore $\boldsymbol{S} = \boldsymbol{F}^{-1} \boldsymbol{\tau} \boldsymbol{F}^{-\mathrm{T}}$ is the second Piola Kirchhoff stress tensor defined in the reference configuration and $\boldsymbol{C} = \boldsymbol{F}^{\mathrm{T}} \boldsymbol{F}$ is the Cauchy-Green deformation tensor, also defined in the reference configuration. Taking advantage of the following expression

$$\frac{\partial \boldsymbol{S}}{\partial \boldsymbol{F}} \boldsymbol{F}^{\mathrm{T}} = 2 \frac{\partial \boldsymbol{S}}{\partial \boldsymbol{C}} : (\boldsymbol{F}^{\mathrm{T}} \boxtimes \boldsymbol{F}^{\mathrm{T}}) \tag{37}$$

and the definition of the second Piola Kirchhoff stress tensor will result in the spatial representation of the tangent stiffness

$$\boldsymbol{\mathcal{L}} = -\boldsymbol{I} \boxtimes \boldsymbol{\tau} - \boldsymbol{\tau} \boxtimes \boldsymbol{I} + \mathrm{sym}_4\left(\frac{\partial \boldsymbol{\tau}}{\partial \boldsymbol{F}} \boldsymbol{F}^{\mathrm{T}}\right) \tag{38}$$

where $\mathrm{sym}_4(\cdot)$ indicates minor symmetry of the fourth-order tensor. In addition, (38) can be rewritten using the relationship $\boldsymbol{\tau} = \boldsymbol{\tau}(\boldsymbol{b}^e, \boldsymbol{m}^\alpha)$. Taking advantage of the fact that $\boldsymbol{F}^p = \boldsymbol{I}$ initially, the initial tangent stiffness is then obtained

$$\boldsymbol{\mathcal{L}}_0 = \left[\frac{\partial \boldsymbol{\tau}}{\partial \boldsymbol{b}^e}(\boldsymbol{I} \boxtimes \boldsymbol{b}^e + \boldsymbol{b}^e \boxtimes \boldsymbol{I}) + \sum_{\alpha=1}^{3} \frac{\partial \boldsymbol{\tau}}{\partial \boldsymbol{m}^\alpha}(\boldsymbol{I} \boxtimes \boldsymbol{m}^{(\alpha)} + \boldsymbol{m}^{(\alpha)} \boxtimes \boldsymbol{I})\right]_{\boldsymbol{F}^e = \boldsymbol{I}} \tag{39}$$

For the calibration process it is assumed that all components are given with respect to the material directions $\boldsymbol{v}_0^{(\alpha)}$. From this assumption it follows that the matrix representation, in Voigt notation, of the initial tangent stiffness is given by

$$[\boldsymbol{\mathcal{L}}_0] = \begin{bmatrix} a_1 + 2c_1 & b_1 & b_3 & 0 & 0 & 0 \\ b_1 & a_2 + 2c_2 & b_2 & 0 & 0 & 0 \\ b_3 & b_2 & a_3 + 2c_3 & 0 & 0 & 0 \\ 0 & 0 & 0 & \frac{c_1 + c_2}{2} & 0 & 0 \\ 0 & 0 & 0 & 0 & \frac{c_1 + c_3}{2} & 0 \\ 0 & 0 & 0 & 0 & 0 & \frac{c_2 + c_3}{2} \end{bmatrix} \tag{40}$$

where the same stacking sequence as in (1) has been used. This expression may then be compared to the classical formulation of orthotropy, where the flexibility matrix is given by (1), i.e. $[\mathcal{L}_0]^{-1} = [\mathcal{C}]$.

By comparing (40) and (1), the involved elastic material parameters can be calculated. It is noted that the parameter related to the first term in (32) is not present in the initial tangent stiffness. The experimental data from out-of-plane compression test is used to calibrate this quantity. By comparing the result from the experiment and a finite element simulation of the compression test, the remaining parameter K_b can be determined. To conclude, taking advantage of (2) in (1) and (40) as well as the properties above, leads to the material parameters related to the elastic properties being given by (all in MPa)

$$
\begin{aligned}
&a_1 = 1719, \quad a_2 = -226, \quad a_3 = 1435 \\
&b_1 = 364, \quad b_2 = 0.5, \quad b_3 = 0.4 \\
&c_1 = 720, \quad c_2 = 720, \quad c_3 = -700 \\
&K_b = 60
\end{aligned}
$$

To model plasticity, as indicated previously, a non-associated plasticity model will be adopted.

As discussed initially, the mechanisms in the in-plane and out-of-plane are very different and it is therefore advantageous to decouple the in-plane response and the out-of-plane response. This makes it possible to introduce a separate plasticity model for the out-of-plane response. For simplicity, however, and to facilitate the in-plane model to be discussed in detail it will be assumed that the out-of-plane response is elastic.

As already indicated, the evolution of the substructure also has to be considered. From (30) it follows that the evolution of the substructure is guided by a potential function. Obviously, the specific choice of potential function for the substructure has to be based on experimental evidence. To the authors' knowledge, such information is not available and would be a very challenging task to obtain. Due to the lack of data it will be assumed that no plastic evolution of the substructure will take place.

From the previous definitions it can be concluded that both the yield function and the potential function were introduced in terms of Kirchhoff stress tensor and structural tensors and were required to be isotropic functions of its arguments. For this purpose the following two types of joint invariants of the Kirchhoff stress tensor and structural tensors are introduced:

$$
\begin{aligned}
I_\alpha &= \boldsymbol{m}^{(\alpha)} : \boldsymbol{\tau} \\
J_\alpha &= \boldsymbol{m}^{(\alpha)} : (\boldsymbol{\tau}^2)
\end{aligned}
\tag{41}
$$

First it is noted that the criterion by Tsai and Wu (1971) has previously been used by de Ruvo et al. (1980) and Suhling et al. (1985) with great success to predict failure of paper based materials. It was also shown by Tryding (1994) that the prediction capabilities could be enhanced if the original Tsai–Wu criterion was modified.

The yield surface is assumed to be of the format given by the Tsai–Wu failure criterion and yield function by Shih and Lee (1978), i.e. to be a linear combination of a quadratic and a linear function in stress

$$
\begin{aligned}
f &= a_1^y(I_1 - I_2)^2 + a_2^y(I_1 - I_3)^2 + a_3^y(I_2 - I_3)^2 + b_1^y(J_1 - I_1^2) + b_2^y(J_2 - I_2^2) + b_3^y(J_3 - I_3^2) \\
&\quad + c_1^y I_1 I_2 + c_2^y I_1 I_3 + c_3^y I_2 I_3 + d_1^y I_1 + d_2^y I_2 + d_3^y I_3 - 1 \leqslant 0
\end{aligned}
\tag{42}
$$

where the linear term is used to distinguish the behavior in tension and compression Here a_i^y, b_i^y, c_i^y and d_i^y, $i = 1, 2, 3$ are assumed to be functions of the internal scalar variables κ_β.

Based on the discussion above, to obtain an in-plane yield surface the following reduction of parameters is used $a_3^y = -a_2^y$, $c_3^y = 2a_3^y$, $c_2^y = 2a_2^y$, $b_1^y = -b_3^y$, $b_2^y = -b_3^y$ and $d_3^y = 0$.

The yield function (42) reduces to

$$
f = (a_1^y + a_2^y + b_3^y)I_1^2 + (a_1^y - a_2^y + b_3^y)I_2^2 - b_3^y I_3^2 + b_3^y(J_3 - J_1 - J_2) + (c_1^y - 2a_1^y)I_1 I_2 + d_1^y I_1 + d_2^y I_2 - 1 \leqslant 0
\tag{43}
$$

To calibrate the material parameters to initial yielding, uniaxial tests can be used as a starting point. Assuming for simplicity that $\|\boldsymbol{m}^\alpha\|$ can be taken as unity in the uniaxial tension/compression tests. Loading in MD is given by $\boldsymbol{\tau} = \pm\tau_{\mathrm{MD}}\boldsymbol{m}^{(1)}$ and in CD by $\boldsymbol{\tau} = \pm\tau_{\mathrm{CD}}\boldsymbol{m}^{(2)}$, the corresponding yield stresses can be found in (3). Tak-

ing advantage of the above loading situations in (43) the parameters a_1^y, a_2^y, d_1^y and d_2^y are found in accordance with

$$
\begin{aligned}
a_1^y &= \frac{1}{2}\left(\frac{1}{\tau_{MD,t}\tau_{MD,c}} + \frac{1}{\tau_{CD,t}\tau_{CD,c}}\right), \quad d_1^y = \frac{1}{\tau_{MD,t}} - \frac{1}{\tau_{MD,c}} \\
a_2^y &= \frac{1}{2}\left(\frac{1}{\tau_{MD,t}\tau_{MD,c}} - \frac{1}{\tau_{CD,t}\tau_{CD,c}}\right), \quad d_2^y = \frac{1}{\tau_{CD,t}} - \frac{1}{\tau_{CD,c}}
\end{aligned}
\tag{44}
$$

As evident from (43), additional loading situations need to be considered in order to calibrate the remaining part of the yield function, i.e. c_1^y and b_3^y. Considering biaxial loading, $\boldsymbol{\tau} = \tau_b(\boldsymbol{m}^{(1)} + \boldsymbol{m}^{(2)})$ it follows from (43) that

$$
c_1^y = \frac{1}{\tau_b^2} - \frac{(d_1^y + d_2^y)}{\tau_b}
\tag{45}
$$

The remaining calibration of initial yielding involve a shear loading condition. Unfortunately, a pure shear test in the MD–CD plane is not an easy task to perform due to the small thickness of the paper. Instead, uniaxial test in 45° to the MD direction is used. For this loading situation $\boldsymbol{\tau} = \tau_{45}(\boldsymbol{e}_1 \otimes \boldsymbol{e}_1)$, where $\boldsymbol{e}_1 = (\boldsymbol{v}^{(1)} + \boldsymbol{v}^{(2)})/\sqrt{2}$ and the last parameter can be found as

$$
b_3^y = -\frac{2}{\tau_{45}^2} + \frac{d_1^y + d_2^y}{\tau_{45}} + \frac{c_1^y}{2}
\tag{46}
$$

It should be emphasized that the 45° loading situation needs to be treated with care since rotation of the preferred directions might take place. Taking advantage of the data from (3), (44)–(46) gives the following initial values for the material parameters in the yield function

$$
\begin{aligned}
a_1^y &= 0.034 \, \frac{1}{\text{MPa}^2}, \quad a_2^y = -0.022 \, \frac{1}{\text{MPa}^2}, \quad d_1^y = -0.060 \, \frac{1}{\text{MPa}} \\
d_2^y &= -0.17 \, \frac{1}{\text{MPa}}, \quad b_3^y = -0.039 \, \frac{1}{\text{MPa}^2}, \quad c_1^y = 0.053 \, \frac{1}{\text{MPa}^2}
\end{aligned}
$$

The shape of the initial yield function is shown in Fig. 8 for the biaxial loading situation. The remaining part is to calibrate the model during plastic loading. Here, two parts are involved; the calibration of the hardening function and the calibration of the potential function. The calibration of the potential function will be addressed first, since the result from this calibration will also influence upon the calibration of the hardening. From (29a) it follows that the plastic part of the rate of deformation tensor is given by the gradient of a po-
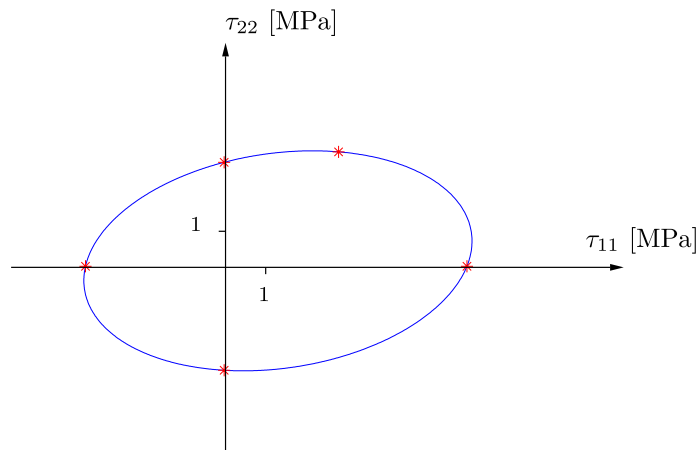

Fig. 8. Initial shape of the yield surface. The solid line represent the initial yield function given by (43) and stars represent the calibration points.

tential function. The potential function guiding the plastic flow direction is based on the yield function and chosen as

$$g = (a_1^p + a_2^p + b_3^p)I_1^2 + (a_1^p - a_2^p + b_3^p)I_2^2 - b_3^p I_3^2 + b_3^p(J_3 - J_1 - J_2) + (c_1^p - 2a_1^p)I_1 I_2 + d_1^p I_1 + d_2^p I_2 - g_r(R_\beta) \tag{47}$$

where a_i^p, b_i^p, c_i^p and d_i^p are material parameters that have to be determined from experimental data. The function g_r will be discussed in the sequel.

As noted in (29) the evolution equations are consistent with the thermodynamic framework if g is a convex function. Hence one needs to establish the restrictions put on the parameters in (47). For this purpose, (47) is written in a coordinate system that is aligned to the material directions. This will result in the following form using matrix representation

$$g = \bar{\tau}^{\mathrm{T}} \begin{bmatrix} a_1^p + a_2^p & (c_1^p - 2a_1^p)/2 & 0 \\ (c_1^p - 2a_1^p)/2 & a_1^p - a_2^p & 0 \\ 0 & 0 & -2b_3^p \end{bmatrix} \bar{\tau} + \begin{bmatrix} d_1^p & d_2^p & 0 \end{bmatrix}\bar{\tau} - g_r(R_\beta) = \bar{\tau}^{\mathrm{T}} A\bar{\tau} + \boldsymbol{d}^p\bar{\tau} - g_r(R_\beta) \tag{48}$$

where $\bar{\tau} = \begin{bmatrix} \tau_{11} & \tau_{22} & \tau_{12} \end{bmatrix}^{\mathrm{T}}$. For the function to be convex in stresses, all eigenvalues to A must be positive, i.e. it follows that

$$b_3^p < 0, \quad a_1^p > \frac{1}{2}\sqrt{(2a_1^p - c_1^p)^2 + 4(a_2^p)^2}$$

must be fulfilled. These constrains must be checked when the parameters are found from the calibration procedure.

Consider next the uniaxial tension tests in MD and CD and the components given in the bases of the material directions. It follows that the plastic part of the rate of deformation can be computed in matrix format as

$$[\boldsymbol{D}^p] = \lambda \begin{bmatrix} 2(a_1^p + a_2^p)\tau_{\mathrm{MD}} + d_1^p & 0 & 0 \\ 0 & (c_1^p - 2a_1^p)\tau_{\mathrm{MD}} & 0 \\ 0 & 0 & 0 \end{bmatrix} \tag{49}$$

when loaded in MD and for uniaxial loading in CD results in

$$[\boldsymbol{D}^p] = \lambda \begin{bmatrix} (c_1^p - 2a_1^p)\tau_{\mathrm{CD}} & 0 & 0 \\ 0 & 2(a_1^p - a_2^p)\tau_{\mathrm{CD}} + d_2^p & 0 \\ 0 & 0 & 0 \end{bmatrix} \tag{50}$$

This allows the following important relations to be established:

$$\frac{D_{11}^p}{D_{22}^p} = \frac{2(a_1^p + a_2^p)}{c_1^p - 2a_1^p} + \frac{d_1^p}{(c_1^p - 2a_1^p)\tau_{\mathrm{MD}}} = H_1$$

$$\frac{D_{22}^p}{D_{11}^p} = \frac{2(a_1^p - a_2^p)}{c_1^p - 2a_1^p} + \frac{d_2^p}{(c_1^p - 2a_1^p)\tau_{\mathrm{CD}}} = H_2 \tag{51}$$

where H_1 and H_2 are given from experimental tests and are referred to as the axial to lateral plastic strain ratios when loaded in MD and CD, respectively. In general, H_1 and H_2 might depend upon the loading. However, a glance of the experimental results shown in Fig. 4, indicate that H_1 and H_2 can be taken as constants for uniaxial loading. Similar experimental findings was found by Stenberg et al. (2001a). As a result, the material parameters d_1^p and d_2^p related to the linear terms in (47) must vanish. Since the potential function is calibrated using axial/lateral plastic ratio, one possible way to calibrate the model is to choose $c_1^p = 1.0$. It is possible in this way to calibrate the remaining two constants a_1^p and a_2^p to the experimental values $H_1 = -3$ and $H_2 = -9.1$. The non-associated format is revealed by comparing the ratio a_1^p/a_2^p to a_1^y/a_2^y. Furthermore, since the remaining parameter, b_3^p is related to shear deformation, and noting the difficulty to preform experiments in shear, this parameter is estimated. Taking advantage of the ratio b_3^y/a_1^y which indicate that magni-

tude of b_3^p should be slightly larger than a_1^p, it will here be assumed that $b_3^p = -1.0$. Using the experimental data discussed earlier, the following values of the material parameters was found

$$a_1^p = 0.60 \ \frac{1}{\text{MPa}^2}, \quad a_2^p = -0.31 \ \frac{1}{\text{MPa}^2}$$

$$c_1^p = 1.0 \ \frac{1}{\text{MPa}^2}, \quad b_3^p = -1.0 \ \frac{1}{\text{MPa}^2}$$

$$d_1^p = 0.0 \ \frac{1}{\text{MPa}}, \quad d_2^p = 0.0 \ \frac{1}{\text{MPa}}$$

The final part of the calibration process concerns the strain hardening of the model. Let us therefore, finally, consider the second term in (31) which is related to the mechanical dissipation. This part becomes important when considering, eg. thermodynamically coupled problems where self heating is of major importance, cf. Håkansson et al. (2005). The thermodynamic format for non-associated plasticity was considered in Ristinmaa et al. (2007) where also the format of Helmholtz' free energy is discussed for isotropic hardening. In this investigation is was conclude that the thermodynamical force is not uniquely defined by only considering the stress–strain response, additional experimental tests were required, such as measure of the stored energy of cold work. As these data are not available and that a thermodynamically coupling is not considered here it will here for simplicity be assumed that $g_r = 0$. This also indicates that ψ^p does not have to be considered.

In Ristinmaa et al. (2007) it was also shown that, as indicated previously, the non-associated format allows the yield function to depend on a very general set of variables. Based on these observations it will here be assumed that the yield function depends on the effective plastic strain, where the evolution of this quantity is introduced according to

$$\dot{\epsilon}_{\text{eff}}^p = \sqrt{\boldsymbol{D}^p : \boldsymbol{D}^p} \tag{52}$$

The hardening functions are then chosen here as

$$\tau_\beta = \tau_0^\beta + k_1^\beta \tanh(k_2^\beta \epsilon_{\text{eff}}^p) + k_3^\beta \epsilon_{\text{eff}}^p \tag{53}$$

where $\beta = 1, 2, \ldots, 6$ are referring to the functions for $\tau_{\text{MD},t}$, $\tau_{\text{MD},c}$, $\tau_{\text{CD},t}$, $\tau_{\text{CD},c}$, τ_{45} and τ_b, respectively, and $k_1^{(\beta)}$, $k_2^{(\beta)}$ and $k_3^{(\beta)}$ are constants. Noted that $\tau_0^{(\beta)}$ corresponds to the initial yield stresses found in (3). To calibrate the hardening behavior, consider first tension loading in MD. From (49) it follows that

$$D_{11}^p = 2\lambda(a_1^p + a_2^p)\tau_{\text{MD}} = \lambda m_1 \tau_{\text{MD}} \tag{54}$$

For the loading situation considered the effective plastic strain rate can be computed from (52) and using (49) as

$$\dot{\epsilon}_{\text{eff}}^p = \lambda\sqrt{4(a_1^p + a_2^p)^2 + (c_1^p - 2a_1^p)^2}|\tau_{\text{MD}}| = \lambda m_2|\tau_{\text{MD}}| \tag{55}$$

Since no rotation of the principal axes take place during the loading it follows that $\boldsymbol{F} = \boldsymbol{V}$, where $\boldsymbol{V}$ is the left stretch tensor in the same manner it is concluded that $\boldsymbol{F}^e = \boldsymbol{V}^e$ and $\boldsymbol{F}^p = \boldsymbol{V}^p$ when the intermediate configuration is selected as an isoclinic configuration. From (54) and (55) it then follows that the plastic multiplier can be eliminated and from time integration it follows that

$$\frac{m_1}{m_2}\epsilon_{\text{eff}}^p = \ln(V_{11}^p) \tag{56}$$

Finally it is noted that the plastic part of the right stretch tensor has to be related to the total stretch tensor since this quantity can be obtained from experimental tests. This can be done by using the definition of the multiplicative split of the deformation gradient. This result in

$$\frac{m_1}{m_2}\epsilon_{\text{eff}}^p = \ln(V_{11}) - \ln(V_{11}^e) \tag{57}$$

The elastic part of the left stretch tensor can be establish since the Kirchhoff stress is related to elastic deformation. Thus (53) can be curve fitted to the experimental uniaxial tests. The calibration process for the other

loading directions follows in a similar manner as above. For the biaxial loading situation a choice of calibration curves has to be made. Here, the CD curve is selected.

Using the experimental data, the following material parameters was found

k_α^β (MPa)	$\beta = 1$	3	5	6
$\alpha = 1$	9.1	3.2	4.1	4.0
$\alpha = 3$	997	190	351	214
k_α^β	$\beta = 1$	3	5	6
$\alpha = 2$	573	366	298	477

Note that the hardening parameters related to compression are not listed since it is assumed that the response in compression is ideal plastic.

3. Numerical examples

Some of the capabilities of the proposed model is demonstrated in this section. The model has been implemented in the finite element code ABAQUS Explicit using the VUMAT interface. The numerical implementation follows within the lines discussed in Harrysson et al. (2007). The calibration procedure of the model is investigated by simulating the experimental setup of the different tests. The results are displayed in Fig. 9. It is clear that the response in the uniaxial tension tests are well captured by the model. Furthermore, the axial–lateral strain is also well captured as evident from Fig. 9(b). When calibration the model to biaxial tension tests, one particular direction has to be chosen in the calibration. As mentioned earlier, here the model is calibrated to CD. Finally, a compression test in ZD is utilized to calibrate the bulk parameter of the elastic
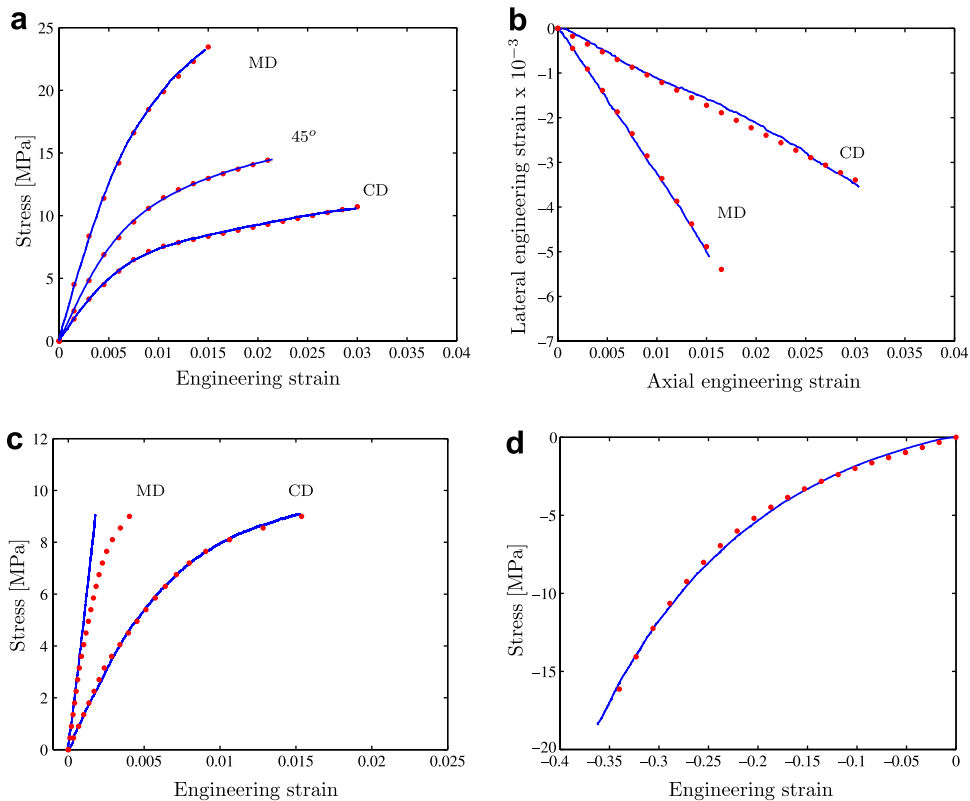

Fig. 9. Comparison of experimental data and the response by the model. Solid line represent experiments and dots represent simulations in all figures. (a) Uniaxial tension test. (b) Axial–lateral strain. (c) Biaxial test using $F_{MD}/F_{CD} = 1$. (d) Compression test in ZD.
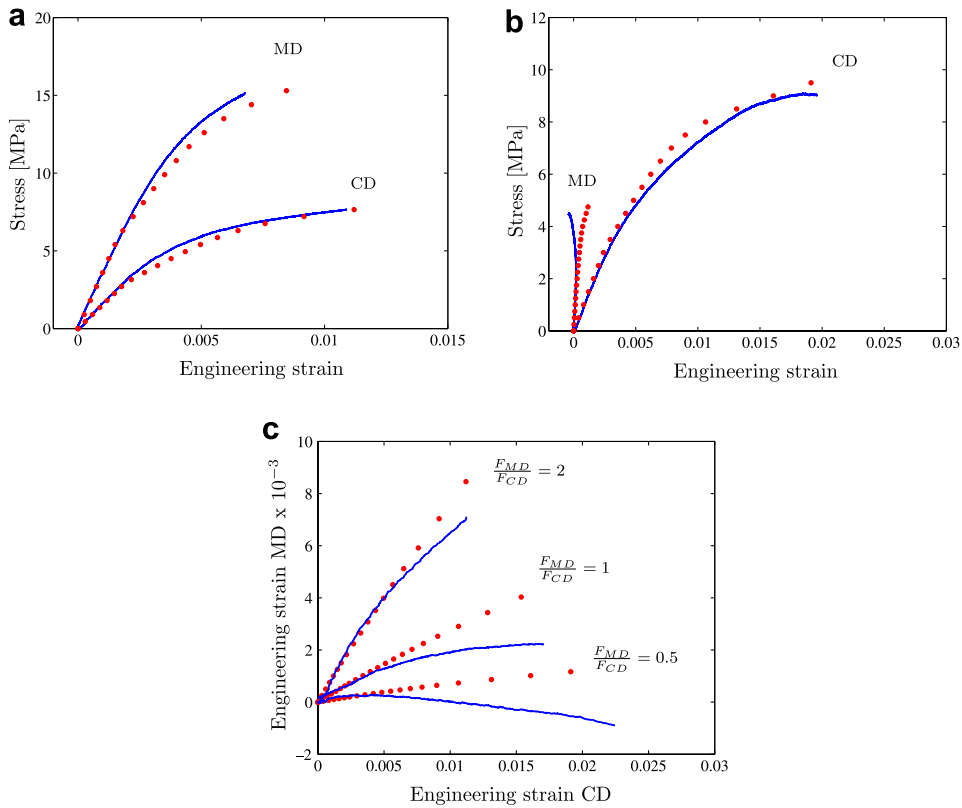
Fig. 10. Simulation of biaxial tension test using (a) $F_{MD}/F_{CD} = 2$, (b) $F_{MD}/F_{CD} = 0.5$ and (c) simulation of MD–CD strain under different biaxial loading situations. Solid line represent experiments and dots represent simulations in all figures.

model. As can be seen in Fig. 9(d), the response is captured well by the model. In addition, simulations of the biaxial tension tests using different loading ratios were carried out. In Fig. 10 additional biaxial tension tests are considered. The two biaxial loading ratios are given by $F_{MD}/F_{CD} = 2$ and $F_{MD}/F_{CD} = 0.5$. Evidently the model does capture the response quite well. To evaluate the model further, the strain components in MD and CD are plotted for the different biaxial load ratios. The results can be seen in Fig. 10(c) which indicates that the strain response to be captured rather well, at least for small strains. Note that for the strain in MD the scale in Fig. 10(c) is exaggerated.

3.1. Creasing of a corrugated board panel

This example is taken from an industrial application involving the creasing of a corrugated board panel. Creases are introduced to achieve a local reduction of the bending stiffness and thus simplify the folding operation and make the corners more clearly distinguish. The creasing of a corrugated board panel is done by letting a punch deform the liner and fluting. A certain force needs to be applied to the punch to be able to perform this crease. In this investigation, a CD crease operation is studied of a corrugated board geometry where the material directions of the paper material are consistent with Fig. 1. The geometry is shown in Fig. 11 where the following geometric data, taken from Nordstrand and Carlsson (1997), is adopted

$$\lambda = 7.26 \text{ mm}, \quad \alpha = 1 \text{ mm}, \quad t_{l1} = 0.211 \text{ mm}$$
$$t_{l2} = 0.169 \text{ mm}, \quad t_f = 0.185 \text{ mm}, \quad t_b = 3.91 \text{ mm}$$

Furthermore, the fluting is assumed to be sinusoidal shaped and the same material properties is assigned to the whole model. During the creasing operation the punch is moved down into the corrugated board panel. To
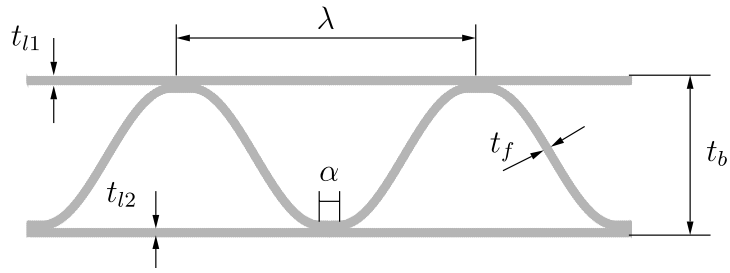
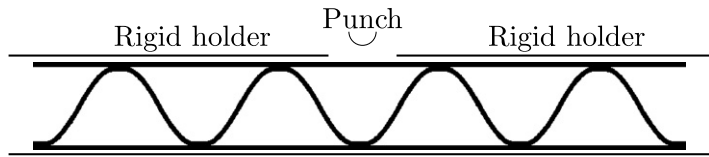Fig. 11. Geometry of a period of a single wall corrugated board panel.

Fig. 12. The overall geometry of a corrugated board panel, together with a punch and rigid holders.

prevent the corrugated board panel to fold during the creasing operation, two rigid holders are placed above the top liner. Here, a board consisting of four wavelength was used, see Fig. 12. The total simulation time was 0.1 s and the punch, 0.5 mm in radius, was moved a distance of $\delta_{\text{punch}} = 3.20$ mm down into the corrugated board panel. Four quadrilateral elements, ABAQUS element type CPE4R, in the thickness direction was used and the total number of elements was 3968. Due to symmetry, only half the structure was modeled. The local behavior of the board during the creasing operation can be seen in Fig. 13. Here the effective plastic strain is plotted to indicate what part on the material undergoes plastic deformation. As expected, the most of the plastic deformation will take place in the fluting. Furthermore, the removal of the punch after the creasing operation results in permanent deformation of the corrugated board panel. The resulting force on the punch during the creasing operation is shown in Fig. 14, where the plateau around 1 mm is due to forming of yield

(a) δ_{punch}=0.64 mm

(b) δ_{punch}=1.28 mm

(c) δ_{punch}=1.92 mm

(d) δ_{punch}=2.56 mm

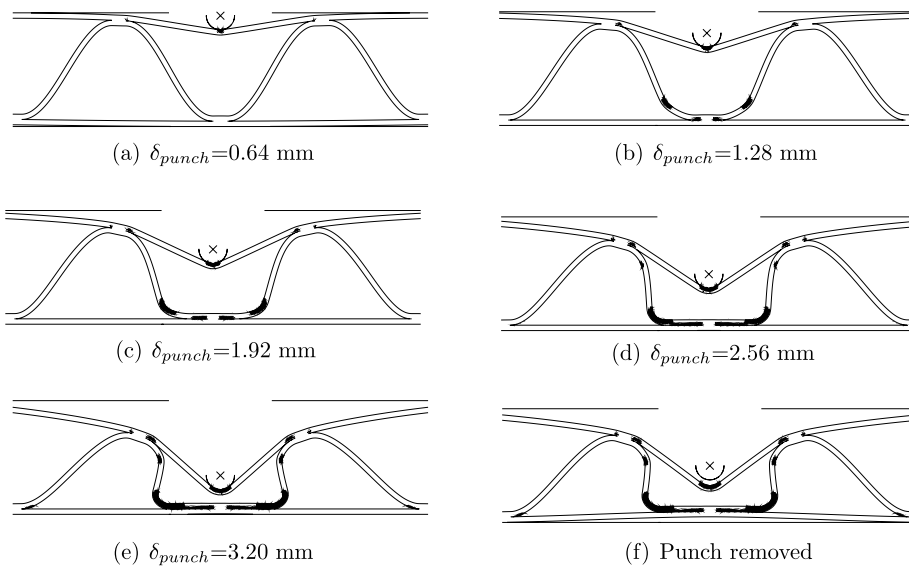(e) δ_{punch}=3.20 mm

(f) Punch removed

Fig. 13. Local deformation of corrugated board during creasing. Dark areas indicates regions where plastic strain exists. The total duration of the creasing process is 0.1 s and the vertical displacement of the punch, δ_{punch}, at the different stage are shown in the figure. Note that in the last stage, the punch has been completely removed.
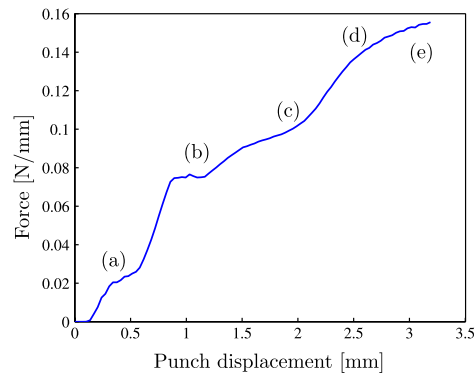
Fig. 14. Force action on the punch during the creasing process. The positions indicated by (a) to (e) corresponds to the deformation patterns in Fig. 13.

hinges in the fluting, cf. also Fig. 13(b). The zero force at the beginning of the loading curve is due to the initial gap between the punch and the board.

4. Conclusion

A large strain orthotropic elasto-plastic model was presented, applicable to corrugated board. It was assumed that the elastic part of the Helmholtz free energy function is described by the elastic part of Finger deformation tensor and the director vectors which represent the preferred directions of the material in the current configuration. To model the anisotropic plastic properties of the material, an yield surface inspired by the Tsai–Wu failure criterion was introduced. This to allow for different yield stresses in the different material directions, but also in tension and compression. Moreover, distortion hardening was utilized to consider different hardening behavior in different material directions. The calibration of the model was also studied in detail. It was found that the model could not be properly calibrated by use of uniaxial tests alone. Thus, biaxial tension tests where preformed using a force controlled setting. The model proposed was implemented into the commercial finite element code ABAQUS/Explicit using the VUMAT interface. To verify the calibration of the model, single element tests were performed for uniaxial loading situations and biaxial loading situations. It was concluded that the calibration procedure worked satisfactorily. Furthermore, simulation of biaxial tests where performed using different loading ratios and the comparison with experimental data show good agreement. A simulation of an industrial application was also preformed were a creasing operation of a corrugated board panel was studied. The result showed considerable plastic deformation of the fluting during the creasing operation. This is also indicated by the remaining deformation of the corrugated board panel, after the removal of the punch.

Acknowledgements

References

Baum, G., 1985. The elastic properties of paper: a review. In: IPST Technical Paper Series. The Institute, Georgia Institute of Technology, Appleton, Wisconsin.
Biancolini, M., 2005. Evaluation of equivalent stiffness properties of corrugated board. Composite Structures 69 (3), 322–328.
Boehler, J., 1987. Applications of tensor functions in solid mechanics. International Center for Mechanical Sciences, no. 292. Springer Verlag, Udine.
Castroa, J., Ostoja-Starzewski, M., 2003. Elasto-plasticity of paper. International Journal of Plasticity 19, 2083–2098.
Cavlin, S., Fellers, C., 1975. A new method for measuring the edgewise compression properties of paper. Svensk papperstidning 78 (9), 321–332.

Ciarlet, P.G., 1988. Mathematical Elasticity, Volume 1: Three Dimensional Elasticity. North-Holland, Amsterdam.

Dafalias, Y., 1986. Issues on the constitutive formulation at large elastic deformations, part 1: kinematics. Acta Mechanica (69), 119–138.

de Ruvo, A., Carlsson, L., Fellers, C., 1980. The biaxial strength of paper. Journal of the Technical Association of Pulp and Paper Industry 63 (5).

Håkansson, P., Wallin, M., Ristinmaa, M., 2005. Comparison of isotropic hardening and kinematic hardening in thermoplasticity. International Journal of Plasticity 21, 1435–1460.

Harrysson, M., Ristinmaa, M., 2007. Description of evolving anisotropy at large strains. Mechanics of Materials 39, 267–282.

Harrysson, M., Harrysson, A., Ristinmaa, M., 2007. Spatial representation of evolving anisotropy at large strains. International Journal of Solids and Structures 44 (10), 3514–3532.

Isaksson, P., Hägglund, R., 2005. A mechanical model of damage and delamination in corrugated board during folding. Engineering Fracture Mechanics 72 (15), 2299–2315.

Isaksson, P., Hägglund, R., Gradin, P., 2004. Continuum damage mechanics applied to paper. International Journal of Solids and Structures 41 (16–17), 4731–4755.

Kröner, E., 1960. Allgemeine Kontinuumstheorie der Versetzungen und Eigenspannungen. Archive for Rational Mechanics and Analysis, 273–334.

Lee, E., 1969. Elastic–plastic deformation at finite strains. Journal of Applied Mechanics 36, 1–6.

Liu, I., 1982. On representation of anisotropic invariants. International Journal of Engineering Science 20, 1099–1109.

Mäkelä, P., Östlund, S., 2003. Orthotropic elastic–plastic material model for paper materials. International Journal of Solids and Structures 40 (21), 5599–5620.

McKee, R., Gander, J., Wachuta, J., 1963. Compression strength formula for corrugated boxes. Paperboard Packaging 40, 149–159.

Menzel, A., Steinmann, P., 2003. On the spatial formulation of anisotropic multiplicative elasto-plasticity. Computer Methods in Applied Mechanics and Engineering 192 (31–32), 3431–3470.

Nordstrand, T., Carlsson, L., 1997. Evaluation of transverse shear stiffness of structural core sandwich plates. Composite Structures (37), 145–153.

Nordstrand, T., Blackenfeldt, M., Renman, M., 2003. A strength prediction method of corrugated board containers. Technical Report TVSM-3065, Div. of Structural Mechanics, Lund University, Sweden.

Nyman, U., 2000. Material and structural failure criterion of corrugated board facings. Composite Structures 50, 79–83.

Patel, P., Nordstrand, T., Carlsson, L., 1997. Local buckling and collapse of corrugated board under biaxial stress. Composite Structures (39), 93–110.

Ristinmaa, M., Wallin, M., Ottosen, N., 2007. Thermodynamic format and heat generation of isotropic hardening plasticity. Acta Mechanica (194), 103–121.

Sawyer, J., Jones, R., McKinlay, P., 1996. An experimental description of the response of paper. Composite Structures (36), 101–111.

Seth, R.S., Page, D.H., 1983. The stress–strain curve of paper. The Role of Fundamental Research in Papermaking – Transactions of the Seventh Fundamental Research Symposium. Mechanical Engineering Publications, Ltd., Cambridge, London, UK, p. 421.

Shih, C.F., Lee, D., 1978. Further developments in anisotropic plasticity. Transactions of the ASME 100, 294–302.

Spencer, A., 1987. Theory of invariants. International Center for Mechanical Sciences, no 282. Springer Verlag, Udine..

Steenberg, B., 1949. Behavior of paper under stress and strain. Technical Section of the Canadian Pulp & Paper Association..

Stenberg, N., Fellers, C., Östlund, S., 2001a. Measuring the stress–strain properties of paperboard in the thickness direction. Journal of Pulp and Paper Science 27 (6), 213–221.

Stenberg, N., Fellers, C., Östlund, S., 2001b. Plasticity in the thickness direction of paper under combined shear and normal loading. ASME Journal of Engineering Material and Technology 123, 184–190.

Stenberg, N., 2003. A model for the through-thickness elastic–plastic behaviour of paper. International Journal of Solids and Structures 40, 7483–7498.

Suhling, J., Rowlands, R., Johnson, M., Gunderson, D., 1985. Tensorial strength analysis of paperboard. Experimental Mechanics, 75–84.

Truesdell, C., Noll, W., 1965. The non-linear field theories of mechanics. In: Flugge, S.S. (Ed.), Handbuch der Physik. Springer Verlag.

Tryding, J., 1994. A modification of the Tsai–Wu failure criterion for the biaxial strength of paper. Tappi Journal 77 (8), 132–134.

Tsai, S., Wu, E., 1971. A general theory of strength for anisotropic materials. Journal of Composite Materials 5, 58–80.

Xia, Q., Boyce, M., Parks, D., 2002. A constitutive model for the anisotropic elastic–plastic deformation of paper and paperboard. International Journal of Solids and Structure 39, 1071–4053.